Real-time imaging of Na+ reversible intercalation in "Janus" graphene stacks for battery applications

CHEMISTRY

Real-time imaging of Na^+ reversible intercalation in "Janus" graphene stacks for battery applications

Jinhua Sun[1], Matthew Sadd[2], Philip Edenborg[3], Henrik Grönbeck[3], Peter H. Thiesen[4], Zhenyuan Xia[1], Vanesa Quintano[5], Ren Qiu[6], Aleksandar Matic[2], Vincenzo Palermo[1,5]*

Sodium, in contrast to other metals, cannot intercalate in graphite, hindering the use of this cheap, abundant element in rechargeable batteries. Here, we report a nanometric graphite-like anode for Na^+ storage, formed by stacked graphene sheets functionalized only on one side, termed Janus graphene. The asymmetric functionalization allows reversible intercalation of Na^+, as monitored by operando Raman spectroelectrochemistry and visualized by imaging ellipsometry. Our Janus graphene has uniform pore size, controllable functionalization density, and few edges; it can store Na^+ differently from graphite and stacked graphene. Density functional theory calculations demonstrate that Na^+ preferably rests close to -NH_2 group forming synergic ionic bonds to graphene, making the interaction process energetically favorable. The estimated sodium storage up to $C_{6.9}Na$ is comparable to graphite for standard lithium ion batteries. Given such encouraging Na^+ reversible intercalation behavior, our approach provides a way to design carbon-based materials for sodium ion batteries.

INTRODUCTION

Lithium ions can intercalate reversibly in graphite with high Li^+ loadings, up to C_6Li, yielding a specific capacity of 372 mA h g^{-1} with the formation of binary graphite intercalation compounds (binary GICs). This nanoscale and reversible process is now at the base of most batteries (*1*–*3*). Sodium would be a cheaper, more abundant alternative charge carrier compared with lithium for batteries, but unfortunately, it can reach only lower loadings in graphite, with a stoichiometry of $C_{64}Na$ and a corresponding capacity of ~35 mA h g^{-1} (*4*–*6*).

The poor Na^+ intercalation was initially attributed to the small interlayer distance of graphite, blocking intercalation of the large sodium ions (*7*, *8*). However, this cannot be the only reason, as experimental evidence shows that potassium ions or solvated Na^+ (e.g., diethylene glycol dimethyl ether solvated Na^+) that are larger than Na^+ can reversibly intercalate in graphite to form binary or ternary GIC, respectively (*9*, *10*–*13*). In contrast with intercalation of bare sodium ions, the co-intercalation of sodium ions with solvent molecules would result, however, in huge volume changes of graphite electrodes and lower specific capacity (ca. 100 to 150 mA h g^{-1}) because the intercalated solvent molecules occupy the space between the graphene layers (*9*, *13*, *14*). The development of novel sodium ion batteries (SIBs) will thus require the intercalation of the bare Na^+ into graphite, without any solvent, in analogy with the bare Li^+ intercalation occurring in current commercial batteries.

The intercalation behavior of sodium ions into graphite is quite unique among alkali (*15*) and alkaline earth metals (*16*–*18*) and has been explained by sodium displaying an unfortunate combination of a relatively low ionization potential and a relatively large ionic radius. The ionization energy of alkali metals decreases moving down the periodic table of elements. For Li, Na, K, Rb, and Cs, it is equal to 5.4, 5.1, 4.3, 4.2, and 3.9 eV, respectively, with a sharp decrease (0.8 eV) between Na and K. A smaller ionization energy favors the formation of an electrostatic coupling between the positive ion and the negatively charged graphene.

Instead, the ionic radius increases moving down the periodic table, increasing from 76 pm for Li^+ to 167 pm for Cs^+. The larger radius means a larger distance between the cation and the graphene, weakening their electrostatic coupling. The interplay between these two opposite trends gives, unfortunately, the weakest chemical binding between Na^+ and graphene among alkali metals (*16*). New strategies fostering (reversible) electrostatic interaction of Na^+ with graphene would lead to a new generation of SIBs.

Here, we describe an artificial graphite nanostructure made of stacked graphene sheets, with the upper face of each sheet being functionalized with a molecule acting both as spacer and as an active site for Na^+ (Fig. 1A). Each molecule in between two stacked graphene sheets is connected by a covalent bond to the lower graphene sheet and interacts through electrostatic interactions with the upper graphene sheet, resulting in a unique structure. The use of asymmetric spacers allows control over noncovalent interactions between the head group of the spacer molecule (in this case, -NH_2) and the graphene surface. Nanosheets having asymmetric chemical functionalization on opposite faces are commonly referred to as "Janus" graphene, named after a two-faced ancient Roman god (*19*).

We were able to confirm the intercalation of Na^+ in the well-defined monoatomic Janus graphene stacks with operando characterizations. Raman spectroelectrochemistry measurements provided real-time observation of the effect of the Na^+ on the vibrational properties of graphene, and operando imaging ellipsometry (IES) allowed tracking of the intercalation process of Na^+ based on the changes in the refractive index of the material. In both cases, the effects are a direct consequence of the intercalation and diffusion of Na^+ between the graphene sheets. The observations in the experiments were confirmed, at the molecular level, by density functional theory (DFT) calculation showing the stability of the Na^+ intercalated in different conformations in the Janus graphene stacks.

[1]Materials and Manufacture, Department of Industrial and Materials Science, Chalmers University of Technology, Göteborg, Sweden. [2]Materials Physics, Department of Physics, Chalmers University of Technology, Göteborg, Sweden. [3]Department of Physics and Competence Centre for Catalysis, Chalmers University of Technology, 412 96 Göteborg, Sweden. [4]Accurion GmbH, Stresemannstraße 30, Göttingen 37079, Germany. [5]Institute of Organic Synthesis and Photoreactivity (ISOF), National Research Council of Italy (CNR), Via P. Gobetti 101, I-40129 Bologna, Italy. [6]Microstructure Physics, Department of Physics, Chalmers University of Technology, Göteborg, Sweden.
*Corresponding author. Email: vincenzo.palermo@isof.cnr.it

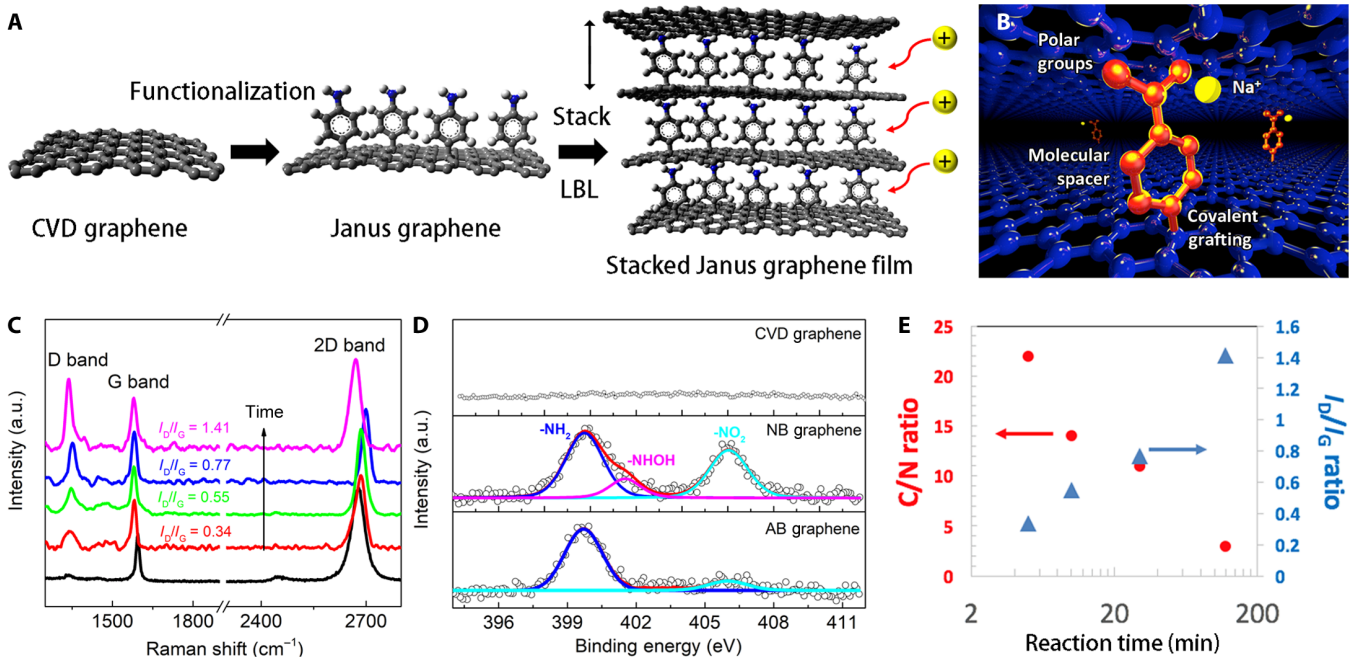

Fig. 1. Preparation of Janus graphene. (**A**) Schematic illustration of the preparation of the Janus graphene and the stacked Janus graphene thin film. (**B**) Cartoon showing Na^+ ions intercalated in between graphene sheets with aminobenzene (AB) spacers. (**C**) Raman spectra of AB graphene featuring different functionalization density, achieved by increasing the reaction time with 4-nitrobenzene diazonium tetrafluoroborate (4-NBD). (**D**) N 1s XPS spectra of chemical vapor deposition (CVD) graphene, NB graphene, and AB graphene. The presence of the $-NH_2$ peak of NB graphene is due to the conversion of $-NO_2$ to $-NH_2$ triggered by x-ray irradiation during the measurement (see also XPS section). (**E**) Simultaneous decrease in C/N ratio (measured by XPS) and increase in I_D/I_G ratio (measured by Raman) with increasing reaction time,

RESULTS

Synthesis of Janus graphene

We used high-quality graphene monolayers grown on copper substrates by chemical vapor deposition (CVD) as a starting material. The upper face of the sheet was functionalized using 4-nitrobenzene diazonium tetrafluoroborate (4-NBD) (Fig. 1A) (*20*). Diazonium chemistry is a very effective approach to graft molecules to graphene by formation of highly reactive aryl radicals, yielding nitrogen gas as the sole by-product (*21*). The density of grafted molecules could be tuned by varying reaction time and temperature (see details in Materials and Methods). After grafting, the nitrobenzene (NB) functional group could be easily converted into an aminobenzene (AB) functional group by electrochemical reduction, thus obtaining two different graphene substrates with the same functionalization density but different surface chemistry: one featuring an electron acceptor $-NO_2$ group, and the other one an electron donor $-NH_2$ group, which could be positively charged in acidic solutions.

The chemical grafting of graphene and the following conversion from NB to AB could be monitored using Raman spectroscopy, cyclic voltammetry (CV), Fourier transform infrared spectroscopy, and x-ray photoelectron spectroscopy (XPS) (Fig. 1, C to E, and figs. S1 and S4D). The change in chemical functionalization was evident also from water contact angle measurements (*22*); the AB and NB functional groups are more hydrophilic than pristine CVD graphene; thus, water contact angle decreased from ca. 83° to ca. 55° for NB graphene and ca. 52° for AB graphene (fig. S2).

Figure 1C shows how the D band, absent in pristine graphene, increased in samples exposed to 4-NBD, indicating the formation of sp^3 hybridization and covalent bonding of the NB group to graphene. The I_D/I_G ratio increased from ~0 to 0.34, 0.55, 0.77, and 1.41 for reaction times of 5, 10, 30, and 120 min, respectively.

We observed a blue shift in the 2D band at low AB functionalization density due to the interaction of the stacked sheets. Different twist angles between layers will affect the Fermi velocity differently, resulting in different degrees of blue shifting in the 2D band (*23*). Noteworthy, for high functionalization density ($I_D/I_G = 1.4$), the density of grafted molecules was so high that it effectively separated the graphene layers, resulting in negligible interaction between the stacked sheets; thus, we observed the 2D band of AB graphene shifting back to its original position. The increase in I_D/I_G ratio was concomitant with an increase in the nitrogen content, measured by XPS as the relative C/N ratio (Fig. 1E; see the Supplementary Materials and table S1 for all details). XPS also allowed monitoring of the chemical conversion of NB to AB by observing the changes in the nitrogen peak (Fig. 1D and the Supplementary Materials for more details).

The diazonium chemical functionalization reaction was, in fact, so effective that for long reaction times, significant self-polymerization took place, with diazonium groups grafting to already reacted molecules (*21*). To reduce issues caused by self-polymerization, we used Na^+ storage test samples with intermediate loading ($I_D/I_G = 0.55$), corresponding to an average distance between AB-grafted molecules of ≈5 nm and a surface density of $\approx 10^{16}$ molecules m^{-2} (see details in Materials and Methods). The presence of physically attached molecules can be excluded because the single-layer Janus graphene film was thoroughly washed by acetonitrile and water after the reaction.

Preparation of stacked Janus graphene films using supramolecular interactions

Once the Janus graphene was synthetized, we needed to stack multiple layers on top of each other. The standard method to transfer and stack CVD graphene sheets is based on a sacrificial poly(methylmethacrylate) (PMMA) layer. This method typically leaves PMMA residues in between the graphene sheets, significantly influencing the graphene stacking and ion intercalation. Instead, we used an original procedure where a first PMMA graphene bilayer was used to "fish," one by one, other layers of graphene freely floating on water after the etching of their copper substrate (Fig. 1A and fig. S3). The procedure could be repeated multiple times until obtaining a PMMA-G_x multilayer, where x was the desired number of graphene sheets, with no contamination in between. Figure 2A shows a typical image of four stacked AB graphene nanosheets underneath one pristine CVD graphene layer. The surface of the film away from the edge is clean without any cracks or holes (fig. S4C). The stacked nanosheets could be clearly recognized even by the naked eye, thanks to their mesoscopic (≈1 cm) size and strong contrast on Si/SiO_2 (Fig. 2A, inset). Raman maps allowed easy discrimination of the different overlapping layers at the sample edges (Fig. 2B). We measured the ratio between the intensities of Raman G and 2D peak (I_G/I_{2D}) (fig. S4). This ratio is typically used to discriminate between monolayer and multilayer graphene, because the shape and intensity of the 2D peak change because of the destruction of the linear dispersion of the electronic bands near the Fermi level when moving from monolayer to multilayers of graphene, as a consequence of the interactions between the layers (*24*–*26*). Also, in our case, the I_G/I_{2D} increased from 0.41 to 0.73 going from G_1 to G_5 multilayers. However, this value was significantly smaller than previously observed in stacked graphene (I_G/I_{2D} = 2.7) (*23*), providing further evidence that the AB molecules act as effective spacers to separate the graphene sheets and thus reduce their interaction. An unexpected yet beneficial advantage of the Janus functionalization was that the reduced intersheet interaction facilitated a better alignment of stacked Janus graphene layers versus pristine graphene, with no noticeable cracks and wrinkles in the stacks, as shown by atomic force microscopy (AFM) (figs. S5 and S6) and transmission electron microscopy (TEM) (Fig. 2, C and D).

AFM measurements of stacked AB graphene yielded a stacking distance of d = 1.2 ± 0.3 nm (fig. S7). The layered structure could also be observed in TEM cross sections, showing the improved and more linear stacking of the AB graphene (Fig. 2C) with respect to the pristine graphene (Fig. 2D). TEM allowed us to estimate a stacking distance of the AB graphene d = 1.7 ± 0.3 nm, significantly larger than what was measured for pristine graphene (d = 0.36 ± 0.03 nm), in agreement with previous reports (*27*). Both AFM and TEM measurements should be taken with caution because of the limited flatness on the mesoscopic scale of the substrate used for the measurements (Si/SiO_2). Nevertheless, the stacking distances obtained by AFM could be compared with the theoretical one of $d \approx 1.2$ nm expected by summing the thickness of pristine graphene (0.34 nm) plus the theoretical length of the AB molecule (0.8 nm). Such a large stacking distance suggests that the grafted AB molecules lay perpendicular between the stacked graphene layers. To better understand the molecular structure of the composite and the possible intercalation of Na^+ ions, we used computational methods.

Multilayer structure and intercalation mechanism of Na^+ studied by DFT calculations

We used DFT calculations to evaluate the preferred configurations of the grafted AB and NB molecules in between the graphene sheets and to compare the energetics of Na^+ intercalation in the material. The results obtained for Na^+ were also compared with Li^+ intercalation (see Materials and Methods and the Supplementary Materials for details). The DFT calculations confirmed a preferential vertical arrangement of the grafted molecules, perpendicular to the graphene sheets, acting as pillars (*8*, *28*, *29*). The optimized distance between

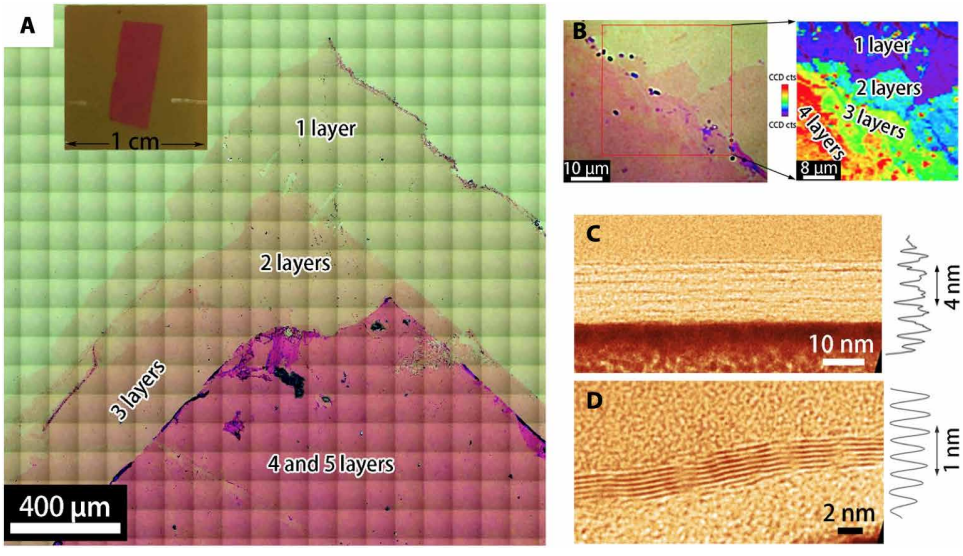

Fig. 2. Characterizations of stacked AB graphene multilayers. (**A**) Optical microscope image of AB graphene multilayers observed at the sample edge. Inset: Macroscopic image of the whole sample on Si/SiO_2. (**B**) Optical microscope image and corresponding Raman mapping of the intensity of 2D band of AB graphene film. (**C** and **D**) Cross-sectional high-resolution transmission electron microscopy (TEM) image of (C) stacked AB graphene thin film and (D) stacked CVD graphene thin film. The averaged intensity profile is reported on the right side of each image.

sheets functionalized with AB was calculated to be 1.0 nm (fig. S11), in agreement with the AFM experimental data. Na^+ and Li^+ showed favorable energetics for intercalation in the functionalized graphene. Calculations of the relative stability of Na^+ in different positions (Fig. 3, A to D, and fig. S12) showed that the most favorable position was obtained having Na^+ coordinated to the -NH_2 group of the AB molecule, while simultaneously in a hollow site in the graphene sheet. The distance between Na^+ and the nitrogen of the -NH_2 group in Fig. 3A was 2.42 Å. The distance between Na^+ and the upper graphene sheet was 2.54 Å, smaller than the ideal sodium graphene distance calculated on pristine graphene (2.64 Å) in the absence of the AB spacer. This suggests a synergic effect of the -NH_2 group and graphene in stabilizing the Na^+. We performed a charge density difference analysis to study the ionic character of the interaction between Na^+, AB molecule, and graphene (Fig. 3E). This analysis showed that the positive charge of the cation is screened by charge accumulation in the graphene sheet. Charge is, moreover, accumulated between the AB group and the Na^+.

Other possible configurations were also tested (Fig. 3, B to D); placing the Na^+ at the bottom of the AB molecule (Fig. 3C), the energy increase with respect to Fig. 3A was +0.49 eV. Placing the Na^+ at the other side of graphene with respect to the AB molecule (Fig. 3B), the energy increase was +0.17 eV. Placing the Na^+ on plain graphene, far from any AB molecule (Fig. 3D), the energy increase was +0.65 eV.

The high stability at the head group was attributed to the synergic polarization of the spacer group and the adjacent graphene. The energy difference between Na^+ coordinated to the -NH_2 group (Fig. 3A) and adsorbed in a conventional position on graphene (Fig. 3D) is significant, but small enough to make diffusion at room temperature frequent also from the most stable site. An estimation using the rate (Arrhenius) expression $r = (k_B T/h)\exp(-\Delta E/k_B T)$ indicates that a barrier energy ≤0.65 eV will allow facile diffusion at room temperature; thus, the site in Fig. 3A will not work as a trap in the material. The computed barriers for Na^+ diffusion were <0.2 eV for AB graphene multilayers, suggesting a facile diffusion of Na^+ in the channels of stacked AB graphene film. The energy calculations thus indicate that once the first Na^+ occupies the position in Fig. 3A, additional Na^+ could be stored in the slightly less favorable positions shown in Fig. 3 (B to D), taking advantage of the large spacing between graphene sheets created by the steric effect of the AB molecule. To confirm this, we performed tests at high Na^+ coverage on smaller cells, with the differential adsorption energy changing only slightly (<0.1 eV) going from NaC_6 to NaC_9, as detailed in Materials and Methods.

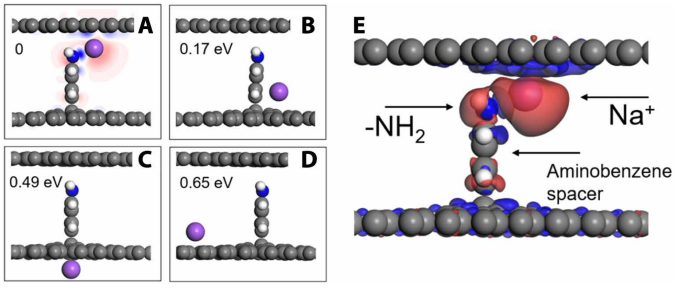

Fig. 3. DFT modeling of Na^+ intercalation in AB graphene. (**A** to **D**) Configurations optimized by DFT calculations for Na^+ intercalation between two graphene sheets separated by AB. The relative energy is indicated with respect to the most stable position in (A). All calculated configurations are reported in Materials and Methods and the Supplementary Materials. Atomic color code: H (white), C (gray), N (blue), and Na (purple). (**E**) Isosurface of differential charge density calculated in presence of Na^+ for the most stable configuration in (A).

Intercalation of Na^+ monitored by operando Raman spectroelectrochemistry

Thanks to the planar geometry and nanometric uniform thickness of Janus graphene film, we were able to monitor directly the intercalation/deintercalation of Na^+ and Li^+ using operando Raman spectroscopy, CV, and IES. First, the method was verified by monitoring Li^+ intercalation in standard materials, i.e., highly oriented pyrolytic graphite (HOPG) and graphene stacks (Fig. 4A). A blue shift of G band, indicative of Li^+ intercalation, was clearly observed in all cases (see also figs. S14 to S17). The same experiment performed with Na^+ showed no shift in neither graphite nor pristine graphene stacks, with a featureless CV spectrum and no noticeable change of Raman peaks (red and black symbols in Fig. 4B; see also figs. S18 to S21).

Na^+ intercalation and deintercalation were instead observed in eight-layer stacks of AB graphene (blue triangle symbols in Fig. 4B), with clear changes in Raman spectra collected operando (Fig. 5A and figs. S22 and S23). The G band started to shift from 1595 to 1605 cm^{-1} at a discharge potential of ~0.6 V versus Na^+/Na (red line in Fig. 5A), attributed to the positive doping of intercalated Na^+ in graphene and a contraction of C—C bonds. The formation of cathodic peak corresponds to intercalation of Na^+ centered at ca. 0.2 V versus Na^+/Na in the CV curve (Fig. 5C).

We studied the effect of AB functionalization density (quantified here as I_D/I_G ratio) on the Na^+ intercalation process. No intercalation (no G band shift) occurred when the I_D/I_G was lower than 0.4 (fig. S24),

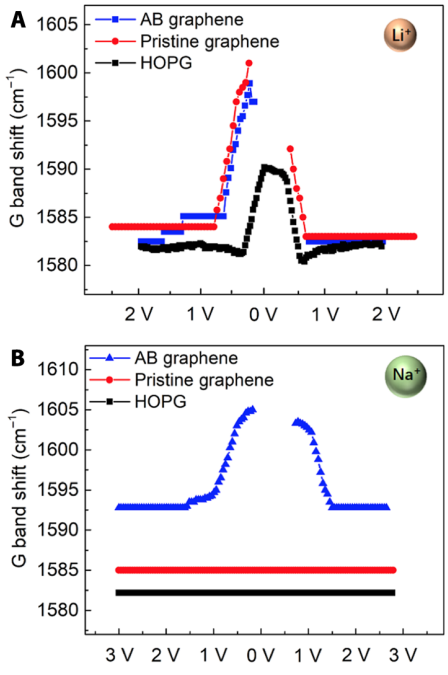

Fig. 4. Comparison of Li^+ and Na^+ intercalation in different materials. (**A**) Shift of G band position during Li^+ intercalation taking place in all materials tested: HOPG, graphene, and AB graphene. (**B**) Same experiment performed with Na^+, showing no intercalation for HOPG and graphene, but intercalation in AB graphene. Some experimental points in the range around 0 V are not reported because the G band decreased so much that it was not possible to measure precisely its shift.

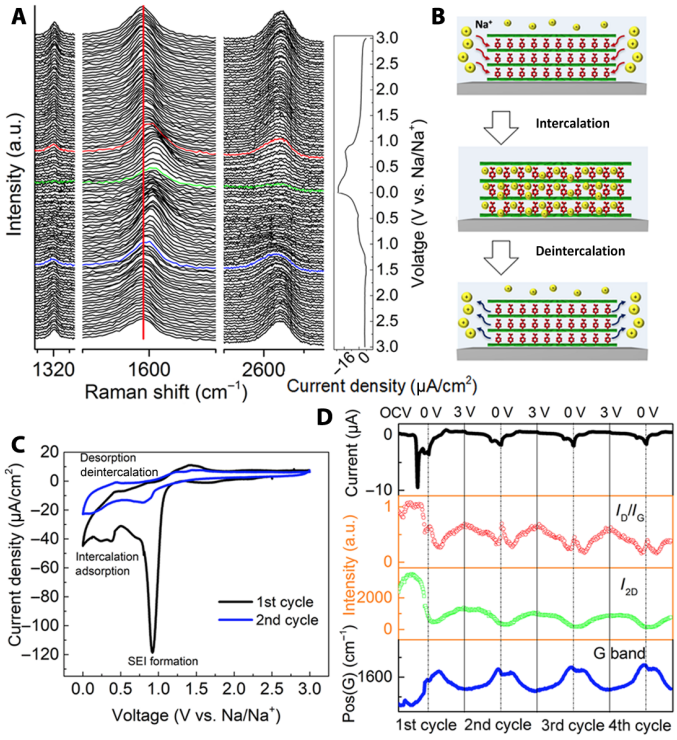

Fig. 5. Monitoring of Na^+ reversible intercalation by operando Raman. (**A**) Series of Raman spectra acquired operando during a complete intercalation/deintercalation cycle of Na^+ in AB graphene; the red spectrum was measured at ca. 0.6 V versus Na^+/Na, green spectrum at 0.05 V versus Na^+/Na, and blue spectrum at ca. 1.5 V versus Na^+/Na. On the right, the corresponding current measured during the cycle. (**B**) A cartoon schematizing the different processes. (**C**) CV curves measured during the first two cycles of Na^+ intercalation in AB graphene. The sweep rate was 0.042 mV/s. The first curve shows a sharp cathodic peak, which disappears in the second cycle, corresponding to the formation of a stable solid electrolyte interphase (SEI). (**D**) Reversible change of different parameters during potential cycling: from top to bottom, we show the measured current, I_D/I_G ratio, intensity of 2D band (I_{2D}), and position of G band.

suggesting that a low density of AB functional groups could not provide enough active sites for the intercalation of sodium ions. Conversely, when functionalization density became too high (I_D/I_G > 1.2), the electrical conductivity was too low to have effective electrical contact between graphene layers, resulting again in poor intercalation of sodium ions. An I_D/I_G between 0.5 and 0.8 thus gave the optimal balance between high electrical conductivity and suitable adsorption sites.

It is noteworthy that in AB graphene, no G peak splitting and no intercalation stages were observed. This is in stark difference with Li^+ intercalation in bulk graphite, which proceeds through many intercalation stages (*30*). Na^+ intercalation in AB graphene showed a direct stage 1 intercalation, indicating that the material had no bulk layers and that intercalation of Na^+ proceeded simultaneously in all stacked sheets.

The coulombic efficiency was low in the first cycle because of the formation of a solid electrolyte interphase (SEI), as evidenced by the difference between the first and second CV curves (Fig. 5C), showing an intense cathodic peak at ~1 V versus Na/Na^+ in the first discharge curve but disappearing in the second discharge curve. This could be expected, considering the tiny mass of the electrode: We had at best eight layers of graphene with an area of ≈0.2 cm^2. As a result of the nanometric mass and large area, the cathodic peak due to the formation of SEI was relatively large compared with the main signal, in agreement with previous works (*31*). The large internal resistance and undesired side reactions caused by the geometry of operando Raman cell result in a large polarization (*32*, *33*). The cathodic peak correlated with the formation of SEI disappeared after the first cycle, indicating the formation of stable SEI layer similar to the graphite for LIBs (Fig. 5C and figs. S27 and S28) (*8*, *34*–*37*). Ex situ XPS comparing pristine and cycled AB graphene showed a large increase in the O peak (fig. S26, A and B), further confirming the formation of an SEI, typically composed of sodium alkyl carbonates (*38*, *39*).

The formation of a stable SEI layer on the entire surface of AB graphene prevents the intercalation of solvent, thus indicating that only bare Na^+ ions reversibly intercalated into AB graphene during the charging/discharging process (*33*, *40*). While the observed spacing of 1.2 nm would be, in theory, sufficient for solvated ion intercalation, the co-intercalation of solvent would result in the exfoliation of Janus graphene layers due to the large size and the decomposition of the solvated molecules for each charge/discharge (*9*). In our sample, no further decomposition of electrolyte was observed after the first discharge for neither lithium nor sodium as evidenced by the disappearing cathodic peak at ca. 0.85 V versus Na/Na^+ (Fig. 5C and figs. S27 and S28). The electrode was intact and stable as evidenced by the periodic change of the current and Raman peaks during the charging/discharging processes (Fig. 5D). No cracks and exfoliated graphene were observed on the surface of AB graphene electrode after discharging, which further demonstrate good structure stability (fig. S26D).

Figure 5D shows the periodic variation of the current and the peak position of the G band as function of potential during four cycles. In addition to the shift of the G band, the intensity of the D, G, and 2D bands also varied with the degree of Na^+ intercalation (Fig. 5D): D and 2D bands monotonously decreased in intensity until vanishing, while the intensity of the G band first increased and blue shifted, and then decreased. The reduced intensity of Raman bands is attributed to the interference of the discrete E_{2g2} mode with a Raman active continuum after the intercalation of ions (*34*). The observed low Raman scattering in turn implies the intercalation of Na ions (*13*, *33*, *41*). All changes in current and G band position were fully reversible, with high cycling stability (Fig. 5, A and D, and figs. S22 and S23) (*42*, *43*). After discharging, the intercalation of Na^+ in the AB graphene electrode was also confirmed by XPS, as evidenced by the presence of intense Na 1s peak at 1069.4 eV (fig. S26B) (*3*). In addition, an N 1s peak was detected from the discharged AB graphene electrode, indicating the good stability of functional groups after reversible intercalation of sodium ions (fig. S26C).

We did not conjecture the presence of superdense Li or Na layer in the material, at difference with what have been observed between two layers of graphene sheets (*1*). This could be excluded because of the large interlayer distance and the presence of dense AB functional groups between Janus graphene layers. Moreover, no cathodic peak deriving from the formation of superdense Li or Na was observed in CV curves, and the Janus graphene electrode showed good reversible charging/discharging stability.

The favorable intercalation of Na^+ is unique for Janus graphene and was not observed on graphene having generic chemical functionalization such as reduced graphene oxide that we tested for

comparison (fig. S25) (*11*). We could estimate the electrochemical performance of Janus graphene film for SIBs based on the CV data (fig. S28). Accurate galvanostatic tests were not possible because of the tiny mass of the electrode. A capacity of ≈332 mA h g^{-1} for Na storage was estimated on the basis of cathodic peaks presented on the fourth cycle of CV curves, almost 10 times higher than that of graphite (35 mA h g^{-1}). The high capacity was attributed to the large interlayer distance and the presence of the active sites for the adoption of Na^+ besides adsorption on the surface of graphene. A stoichiometry of $C_{6.9}Na$ was obtained for AB graphene, which was comparable to values seen for graphite with lithium (C_6Li). We propose some possible reaction related to the storage of sodium ions in AB graphene electrode (fig. S28) and show the corresponding processes in Fig. 5C. It is noteworthy that the number of ions stored (1 Na^+/6.9 C atoms) is significantly larger than the total number of AB molecules in the composite, estimated by XPS (one AB/34 C atoms; see table S1). This suggests that Na^+ is not stored uniquely at AB functional groups; as shown in Fig. 3 (A to D), also other sites can be active to absorb Na^+, with graphene playing a relevant role in the sodium ion storage. The functional groups do not only act as ion traps but also make the Na^+ easier to intercalate in other positions, due to the enlarged interlayer distance and favorable binding energy.

Visualization of Na^+ intercalation process

To track the spatial evolution of Na^+ intercalation in AB graphene film on a microscopic scale, we used electrochemical operando IES. The IES technique records of the ellipsometric angles Δ and Ψ micrographs at different orientation of polarizer and analyzer (Fig. 6). Δ is the phase difference of the light before and after being reflected by the different interfaces of the sample, and Ψ is the amplitude ratio of p and s (linear and orthogonal) components to the light incidence plane. The ellipsometric angles are highly sensitive to changes in refractive index and layer thickness and have been recently used to measure graphene-polymer stacks on mesoscopic scales (*44*).

Figure 6 (A and B) shows microscopic maps of Δ recorded while electrically biasing the sample and corresponding charging/discharging curve. Figure 6C shows the values of Δ and Ψ averaged on all pixels plotted against time and voltage variation, showing a clear correlation with the CV current and thus with Na intercalation/deintercalation. The ellipsomeric angle Δ varied as the de-/intercalation of Na^+, which was indicated by the color change between red and blue (Fig. 6, A and B). The changes of Δ and Ψ are Na^+ concentration dependent between the AB graphene layers. As more sodium ions intercalated, the optical density increased because the interlayer was filled gradually with the sodium ions. Thus, the composition and the surface properties of Janus graphene interlayers changed, which result in the variation of the Δ and Ψ at different wavelength and angle of incidence. Animated movies showing the intercalation process, obtained combining together >500 single ellipsometry images, are available in the Supplementary Materials. There is thus a direct correlation between the changes in Δ and Ψ shown in Fig. 6A and the intercalation of Na^+ in the material.

The simplest way to explain this result would be to attribute them to changes in layer thickness of the graphene stacks, due to Na^+ intercalation, as typically observed in many GICs. However, the radius of the Na^+ ion is 0.102 nm, much smaller than the sheet spacing

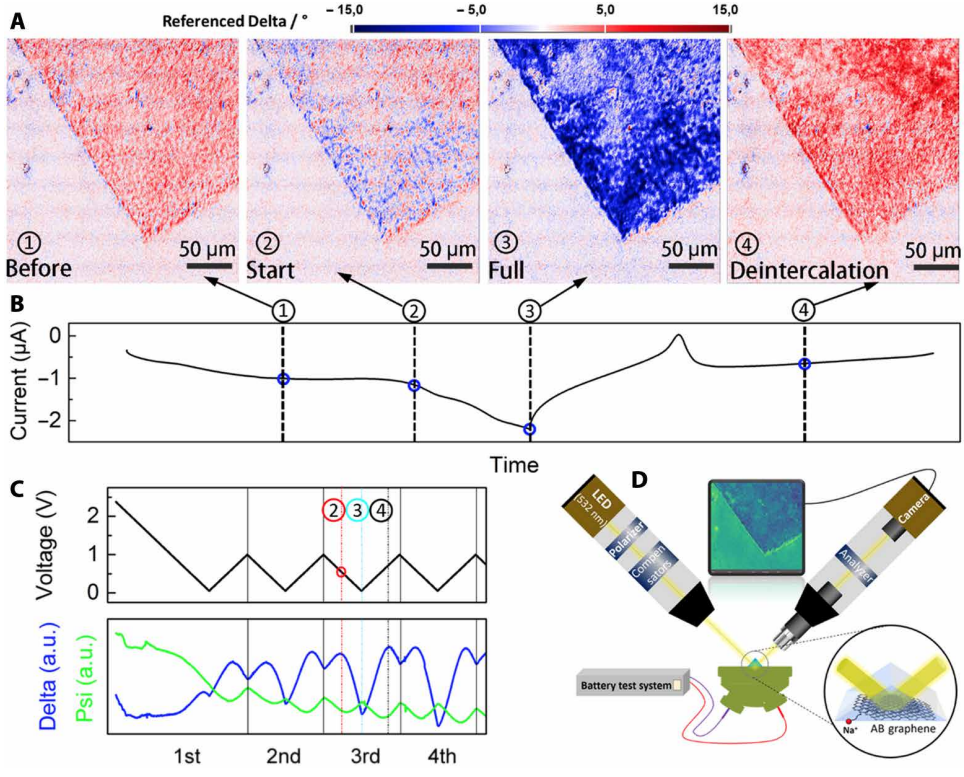

Fig. 6. Tracking the Na^+ reversible intercalation into Janus graphene electrode by IES. (**A**) Maps displaying the changes in the ellipsometric angle Δ obtained by IES during Na^+ intercalation/deintercalation in AB graphene. (**B**) Corresponding current-time profile of the intercalation/deintercalation process. (**C**) The periodic change of voltage, Δ, and Ψ during intercalation/deintercalation processes. (**D**) Schematic illustration of the IES setup.

available in the Janus graphene (1.2 ± 0.3 nm). A more likely explanation is based instead on changes in the optoelectronic properties of the material, with an increase in the refractive index of the material due to the large number of charged ions entering between the sheets.

To confirm this hypothesis, we used an optical modeling software (nanofilm_EP4, Accurion) to perform a simplified simulation of the ellipsometric angle Delta for three charging/discharging cycles. The model included a stack of eight layers of graphene and an interlayer stack in-between. A glass substrate was set on the stack, and an effective medium with a volume fraction of 0.5 of the main components of the electrolyte solution was set under the stack. The simulation can be considered qualitative because it did not include additional layers like SEI nor the ions in the electrolyte and did not reproduce the fine structure of the AB groups present in the Janus graphene. It is not possible to perform a quantitative simulation of the ellipsometric angles because of the uncertainty in estimating the changes in the refractive index due to sodium ions present in the void interlayer space, interacting with the delocalized electron system of the graphene layers and other sodium cations. To model the interlayer space, we thus used a Bruggeman effective medium approximation for the refractive index. We calculated the ellipsometric Delta for an increasing volume fraction of sodium in between the graphene stacks, with the remaining volume being filled by a host (air). Figure S30 shows the full three-dimensional representation of the ellipsometric Delta, calculated varying the volume fraction of sodium in between the layer and the thickness of the void interlayer between the graphene sheets. Figure S30B shows how Delta is expected to vary by adding or removing Na in between the graphene layers to mimic the real charging/discharging processes. We calculated also Delta for different thickness of the void interlayer space. By tuning interlayer spacing and Na content, we could reproduce in a qualitative way the experimental data (Fig. 7A). The best fit is shown in Fig. 7B and was obtained assuming a stack periodicity of 0.643 nm (0.34 nm of graphene + 0.30 nm of void interlayer space). This is half of the experimental measured thickness (1.2 nm) but, given the strong approximations of our simplified model and the good agreement in the observed charge/discharge trends, confirms that the cycled introduction/extraction of sodium in between Janus graphene could explain the observed IES data.

A full quantitative understanding of the IES data would require a theoretical modeling of the refractive index of this nanocomposite structure formed by graphene, organic molecules, and metal ions, which is beyond the scope of this paper, and a possible goal for future works would require additional data from spectroscopic IES.

We could observe on a macroscopic scale that changes began most often from the edges of the sample (Fig. 6A), confirming the high quality of Janus graphene layers, excluding the presence of holes or cracks on the graphene surface that would act as preferential paths for intercalating ions. Thus, this unique structure allows us to readily track the interaction and diffusion of sodium ion along the macroscopic planar electrode from the edges of stacks by imaging.

The surface, edges, and empty pores can be a significant part of the active materials and have a significant impact on the lithium/sodium ion storage, especially in the case of disordered materials with high surface area, like activated carbon (*45*). In contrast, our samples feature an extremely low amount of edges. For a typical stacked Janus graphene, the lateral edge of the 0.2*0.5 cm^2 electrode is $1.4*10^{-2}$ m for a mass of few nanograms. For comparison, an equivalent amount of graphene flakes having the same thickness d = 8 layers and a flake radius r = 500 nm would have a total flake edge $>10^4$ m [estimated using the formula $L_{edges} = 2M/(\rho r d)$, where M is the mass of the material, ρ is the density, and the flakes are approximated as perfect circles of radius r and thickness d]. The effect of surface edges in Janus graphene film is in this way minimized as compared with an equivalent amount of disordered material in powder. Thus, the macroscopic size of the CVD graphene sheets and their perfect stacking allow the reduction of the influence of edges in the samples of six orders of magnitude as compared with an equivalent amount of disordered material in powder.

DISCUSSION

The structure of graphene with only one surface being functionalized can be unique as compared with the one symmetrically functionalized on both sides. The surface properties abruptly changed after introducing a functional group, while the geometry of the opposite surface is preserved. This controllable surface change allowed us to prepare stacked Janus graphene layers with much better alignment versus pristine graphene, due to the weak interlayer interaction, and

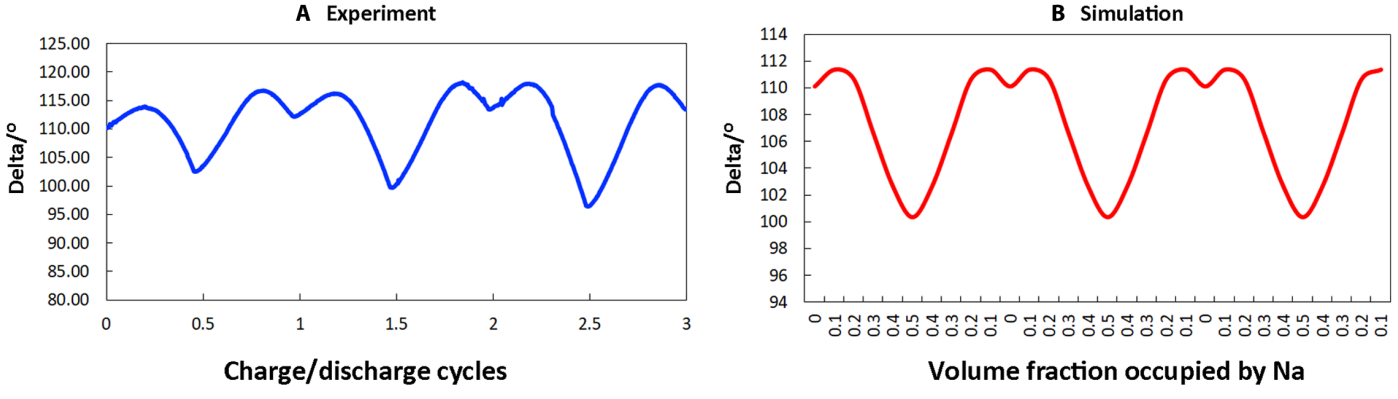

Fig. 7. Simulation of the ellipsometric angle Delta. (**A**) Experimental values of ellipsometric Delta measured during three charge/discharge cycles (taken from Fig. 6C). (**B**) Simulated values of ellipsometric Delta obtained cycling three times from 0 to 0.5 volume fraction of sodium ions, with a thickness of the void space between two graphenes of 0.30 nm.

use the prepared films as a model system to understand the intercalation of sodium ions into graphite-based materials.

The Janus graphene has a uniform intersheet pore size and a minimal amount of edges, thanks to the choice of macroscopic CVD graphene sheets. Although the chemical group is attached only on one side of the graphene, it will also influence the other, nonfunctionalized side (*19*) and the graphene sheet stacked directly above it, as indicated by DFT calculations, forming thus a complex 3D site that can stabilize Na^+ ions more effectively than pristine graphite.

The Na^+ storage behaviors observed in Janus graphene are different from what happens in highly crystalline graphite with Li^+. Instead of proceeding through a sequence of increasing intercalation stages (from stage 4 to stage 1) (*41*), a direct stage 1 intercalation mechanism for sodium ions was observed in Janus graphene, with no intermediate intercalation stages (e.g., stage 4). This evidence is not compatible with the classical process always used to describe ion intercalation in graphite. At difference with studies of highly disordered carbons, a reversible shift of G band and an intensity change of the 2D band could be observed in the Raman spectra of Janus graphene. These changes could be observed clearly in our ordered stacks and not, as example, in more disordered and defective graphenes, such as reduced graphene oxide (fig. S25) (*11*). The presence of AB molecules has also a clear, significant influence on the intercalation behavior, because Na^+ intercalation was not observed in pristine graphene reference samples (Fig. 4C and fig. S21). This beneficial effect was explained by DFT calculations (Fig. 3), which also indicate that the storage process is related to the presence of the AB groups and, in particular, the most favorable storage configuration.

In summary, experimental results obtained by independent techniques indicate that the asymmetric functionalization of graphene with AB molecules yields a layered structure where the AB act as spacers increasing the distance and minimizing the van der Waals interaction between the graphene sheets. DFT calculations indicate that AB molecules are covalently grafted to graphene in a vertical position, with the $-NH_2$ groups forced to stay in close proximity to the adjacent graphene sheet, with a fixed orientation respective to it. DFT calculations also show that these active groups have a synergic effect with graphene to stabilize Li^+ and, more importantly, Na^+ ions in the stacked Janus graphene film. Owing to the high quality of the CVD graphene used, the planar geometry, the good control on the functionalization chemistry, and a clean stacking procedure with no polymer contamination, we could perform Raman, CV, and IES experiments operando during charging/discharging processes for SIB. These experiments confirmed the DFT results showing that the AB graphene can be intercalated/deintercalated with Na^+ ions in a reversible and stable way, in contrast to graphite or stacked graphene, differently from other materials studied for SIBs. We expect that the present research about Janus graphene could provide a proof of concept of using asymmetrically functionalized artificial graphite for the application of SIBs.

MATERIALS AND METHODS

Synthesis of NB-functionalized CVD graphene

CVD graphene was purchased from Graphenea, Spain. 4-NBD was purchased from Sigma-Aldrich or synthesized following the procedure reported in (*43*). All other chemicals and solvents were purchased from commercial suppliers (Sigma-Aldrich and VWR) and used without further purification. The functionalization of CVD graphene was carried out by immersing CVD graphene/Cu in 4-NBD aqueous solution under different concentrations (0.001 to 50 mmol). The surfactant sodium dodecyl sulfate (SDS) was added in the solution to allow 4-NBD to have better solubility in water and contact with the surface of graphene. To control the density of NB functional groups on the surface of CVD graphene, the CVD graphene was immersed for different periods of time (from 1 to 120 min) as detailed in table S1. After reaction, the NB-functionalized CVD graphene was thoroughly washed by deionized water, acetone, chloroform, and acetonitrile.

In our unique approach, the chemical functionalization was performed on the top surface of the CVD graphene while the bottom surface is still tightly adhering to the copper substrate where it was grown. After the functionalization, the copper protective layer was etched in a different solution (i.e., 0.1 M ammonium sulfonate solution), not containing any 4-NBD precursor; thus, any chemical functionalization of the lower surface could be excluded.

Electrochemical conversion of NB functional group to AB functional group

The nitro group in NB-functionalized graphene was electrochemically reduced to amino group in 0.1 M KCl in the mixture of water/ethanol (9:1 in volume). Figure S1 shows the typical CV curves of the electrochemical reduction of NB to AB. The presence of a reduction peak at about −1 V versus Ag corresponds to the reduction of nitro functional groups to amino functional groups. This reduction peaks disappeared after the first cycle, indicating the efficient conversion of nitro groups to amino groups.

Electrochemical reduction was performed using a potentiostatic method with a three-electrode system. The NB-functionalized CVD graphene was first flushed with water and electrolyte: 0.1 M KCl in the mixture of water and ethanol (9:1) before being immersed in the electrochemical cell. A silver wire was used as reference electrode and a Pt foil was used as counter electrode. The NB-functionalized graphene on Cu was used as working electrode and was cycled three times from −0.3 to −1.3 V under a scan rate of 50 mV/s. The reduction was almost complete after the first cycle, with a big cathodic peak at about −1 V versus Ag. Then, the surface was thoroughly rinsed by DI water and acetonitrile.

Assembly of single-graphene sheets to prepare stacked multilayers

The standard graphene transfer procedure is performed using a PMMA sacrificial layer, deposited on graphene by spin coating, and then the underlying copper substrate is etched. The PMMA-G bilayer is transferred on the target substrate, and lastly, the PMMA is dissolved in a solvent. This standard transfer method is effective but tends to leave contaminations of PMMA on the surface of graphene, which could influence significantly the stacking of multiple graphene sheets.

Thus, instead of using PMMA as supporting layer to transfer each layer of Janus graphene, we used an alternative method by coating PMMA only once, on the first layer of graphene (*23*). This first PMMA-G bilayer was then used to fish, one by one, other layers of graphene freely floating on water after the etching of their copper substrate (see fig. S4).

The procedure was as follows: a thin layer of PMMA was spin coated on the surface of graphene (2000 rpm for 1 min). After coating PMMA, the CVD graphene/PMMA was heated on a hot plate for 10 min at 120°C. The copper was etched by floating the film on

0.1 M ammonium sulfonate solution for at least 5 hours. After washing by using DI water to remove all the absorbed ions on the surface of graphene, a fresh NB or AB-functionalized graphene film was used as substrate to deposit the floating graphene/PMMA on it. Thus, no PMMA contamination was present between the layers. The sample was dried in air overnight.

The procedure could be repeated multiple times until obtaining a PMMA-G_x multilayer, where x was the desired number of graphene stacks. This novel strategy allowed to have multiple stacks without any PMMA contamination between graphene layers. The final stacked multilayer graphene film could be transferred to any substrate (e.g., glass, Si/SiO_2) for test and Raman characterization (fig. S4). After transfer to the target substrate, the top layer PMMA was removed by acetone vapor.

The surface of the pristine graphene was hydrophobic and became significantly more hydrophilic with functionalization, as demonstrated by contact angle measurements (fig. S2). An unexpected advantage of this functionalization was that it fostered a better wetting thin layer of water once trying to fish the graphene on water. We found that the hydrophilic surface facilitates a better alignment of stacked Janus graphene layers, likely maintaining a lubricating layer of water at the interface, resulting in high-quality stacks and surfaces with no noticeable cracks and wrinkles, as shown in AFM images of two, four, and six stacks (fig. S5). Conversely, the same procedure applied on pristine graphene yielded much worse stacking, with randomly oriented wrinkles observed already in G-G bilayers (fig. S6). This suggests that the presence of our grafted molecular spacers allows a better sliding, likely fostered by water, between the interlayers. In contrast, the strong van der Waals interaction between CVD graphene layers results in closer contact between graphene layers, preventing the fast evaporation of water and leading to the formation of wrinkles.

Stacking CVD graphene to prepare pristine CVD graphene thin film

The stacks of pristine CVD graphene thin films were prepared following the same procedure as the stacks of Janus graphene thin film. However, for the stacking of CVD graphene, the surface tension of water was tuned by adding isopropanol to obtain a relatively flat film as reported previously.

Materials characterization

XPS data were collected using PHI 5500 by PerkinElmer (Waltham, Massachusetts, USA) with monochromatic Al Ka source (1486.6 eV) with 100-μm spot size. All XPS data were analyzed and quantified using PHI MultiPak Software. Raman analysis was carried out using a WITec alpha300 R (532-nm laser) spectrometer operating at low power. TEM images were acquired on an FEI Tecnai T20 LaB6 with an electron acceleration energy of 200 kV; TEM sample for the cross-sectional measurement was prepared by focused ion beam (FEI Versa3D LoVac DualBeam).

AFM (Bruker Dimension 3100) was used to characterize the surface and the thickness of AB graphene, NB graphene, and stacked CVD graphene film in tapping mode in air. For the thickness measurement, the film was scratched by a sharp tweezer tip. Static contact angle measurements were obtained using a Theta contact angle meter from Biolin Scientific. The water contact angles were recorded at 15 frames per second and were determined within 1 s after adding 2 μl of deionized water to, for example, AB graphene. Average values of three measurements were reported. IES was performed using a commercial EP4 setup (Accurion GmbH, Gottingen) in polarizer compensator sample analyzer (PCSA) configuration. The difference to a conventional ellipsometer setup is the inserted objective and charge-coupled device (CCD) camera to enable imaging capabilities. The EP4 is equipped with a monochromator that provides monochromatic light with variable wavelength (λ) in the range of 250 up to 1700 nm.

Operando Raman spectroelectrochemical characterization

The commercial EL-CELL Raman cell (fig. S14) was assembled in the glove box using graphene stacks deposited on glass disc as working electrode, glass fiber as separator, and lithium and sodium metal as counter electrode for LIBs and SIBs, respectively (fig. S14). For each measurement, the size of a typical stacked eight-layer Janus graphene thin film is about 0.2*0.5 cm^2. All potentials reported were measured against Na/Na^+ electrode for Na^+ intercalation and Li/Li^+ electrode for Li^+ intercalation under a two-electrode system, respectively. For lithium ion intercalation, 1 M $LiPF_6$ in ethylene carbonate and diethyl carbonate (EC/DEC) was used as the electrolyte; for sodium ion intercalation, 1 M $NaPF_6$ in ethylene carbonate and dimethyl carbonate (EC/DMC) was used instead. To achieve a good electrical contact with the graphene, a nickel foil disc with an opening in the middle was used as current collector. A 632-nm incident laser was focused on the back side of Janus graphene electrode through the glass disc and in the opening on the copper current collector. A single Raman spectrum was recorded every 20 min during the charging/discharging of the cell. CV was performed to induce electrochemical intercalation/deintercalation of sodium ions using a Gamry Reference 600. A low scan rate of 0.042 mV/s was applied, which allowed Raman spectra to be collected at quasi-equilibrium conditions. The capacity was obtained by a standard integration method of the cathodic peak in the fourth cycle of CV curves (fig. S28), which is related to the intercalation of sodium ions to exclude any side reaction (e.g., SEI formation).

DFT calculations

DFT calculations were performed with the Vienna Ab-Initio Simulation Package (VASP) (*46*–*49*) using the projector-augmented wave method to describe the interaction between the valence electrons and the core (*50*). The numbers of valence electrons treated explicitly were H (1), Li (1), C (4), N (5), and Na (1). The Kohn-Sham orbitals were expanded using a plane wave with a cutoff energy of 500 eV. The exchange-correlation functional was approximated with the Perdew–Burke–Ernzerhof (PBE) formula (*51*) augmented with the D3 approach to capture van der Waals interactions (*52*). The integration over the Brillouin zone was approximated with finite sampling. The structures were optimized using the Atomistic Simulation Environment (*53*) until the largest force was below 0.02 eV/Å. The lattice constant for a graphene sheet was optimized to be 2.46 Å, which coincides with the experimental value.

The intercalation energies of Li and Na as a function of interlayer distance between two graphene sheets are shown in fig. S10. These results are calculated using a (3 × 3) graphene surface cell and an AB stacking of the two sheets. The adsorption energy is computed as the difference between the energy of the considered system and the energy of the metal atom in the bulk and the two graphene sheets in vacuum. A negative adsorption energy corresponds to exothermic adsorption. We find that the optimized interlayer distance for Li is 4.1 Å, whereas it is 4.9 Å for Na. The process is strongly endothermic

for Na at the interlayer distance corresponding to the preferred distance for two sheets (3.60 Å).

The preferred interlayer distance of two graphene sheets in the presence of an AB functional group was studied using a (6 × 6) surface cell. Thus, there are 72 carbon atoms in each graphene sheet, and the Na/C ratio is 1/72. The results are shown in fig. S11. The energy is in this case a balance between the interactions between the graphene sheets and the interaction between the spaces and the two sheets. A small interlayer distance favors the layer-layer interaction as well as the interaction between the layers and the benzene ring. However, a small distance introduces strain in the bond linking the spacer molecule and the graphene sheet. An optimized interlayer distance is found at 10 Å.

We tested, for comparison, the stability of Li^+ and Na^+ for the NB-functionalized spacer. All configurations tested are shown in fig. S12, with the corresponding energy value calculated for each combination of ion (Li^+ or Na^+) and end group (NO_2 or NH_2). Both -NO_2 and -NH_2 groups significantly stabilize the intercalated Li^+/Na^+ ions; as expected, the electron-rich NO_2 group of NB showed an even stronger interaction with both Li^+ and Na^+ than the electron-poor NH_2 group of AB.

The cations are preferably bonded to the -NH_2 or -NO_2 group of the ligand. This storage site (Fig. 3A) is clearly preferred with respect to storage on the graphene layer (e.g., Fig. 3D). The differences in the relative stabilities reflect the absolute bond strength. The bond to the Li^+ is stronger than that of the Na^+ (fig. S12). The bond strength of Li^+ with respect to Li in the metal phase is calculated to be −0.81 eV in configuration of fig. S12A with the NH_2 group. The corresponding value for Na^+ is −0.71 eV. In the case of the NO_2 group, the bond strength with respect to the metal is calculated to be −1.26 and −0.86 eV for Li^+ and Na^+, respectively.

We also performed additional calculations on the coverage dependence of Na^+ storage between graphene sheets for higher storage densities, up to NaC_6. The calculations were performed on a smaller 3 × 3 cell having graphene sites preoccupied by Na^+ ions. We found a very weak coverage dependence, with the differential adsorption energy changing <0.1 eV going from NaC_6 to NaC_9.

Figure S13 compares the charge transfer between Na and the graphene sheet with and without AB spacer, analyzed by calculating the charge density difference. The difference is computed with respect to the neutral atom and the corresponding graphene structure. The iso-surface at 0.007 e/$Å^3$ is visualized. The analysis demonstrates that charge is transferred from the Na atom forming an ionic bond to the sheet. The analysis is consistent with a Bader charge analysis (*54*, *55*) revealing that the Na atom has a positive charge of about 0.9 e. The charge transferred to the graphene sheet is localized closed to the cation.

Operando IES

The dynamic intercalation process of sodium ions into Janus graphene was investigated in spatial and time resolution using electrochemical operando IES. To avoid the interference of SEI formation and side reaction, which could also cause the variation of thickness and optical parameters of Janus graphene thin film, the new cell was first discharged to 0.05 V versus Na/Na^+ from open circuit voltage and afterward charge/discharged between 1 and 0.05 V versus Na/Na^+.

IES was performed with a nanofilm_EP4 (Accurion GmbH, Goettingen Germany). The instrument is equipped with a GigE CCD camera (1392 × 1040 pixel, 12 bits) as a detector. The light source for time-depending measurements was a light-emitting diode (LED) at 532 nm, selected from a high-power multiwavelength LED Hub. The microscopic maps were recorded at an angle of incidence of 45°. The microscopic magnification was realized by a 20× objective, and for overall focusing, the focus scanner of the instrument was used. The ellipsometric lateral resolution of the imaging system is 1 μm.

The AB graphene sample was placed, and the EC-CELL (fig. S14) was assembled in the same way as described for Raman experiments. In addition, a glass prism (BK7, 90°, 5 × 5 mm) was mounted on top of the glass window of the EL-cell using a thin immersion oil film.

The microscopic maps and numerical data were recorded in parallel. The calculation of referenced maps was performed with the software page "Ep4_datastudio" (Accurion GmbH).

Even without the optical modeling, the changes in the ellipsometric angle are significant, and the variation is significantly larger for AB graphene than for a nonintercalating sample and also for areas in the field of view without graphene. The results demonstrate that IES has high sensitivity to voltage-related Na^+ intercalation under in situ conditions. The lateral resolution allows to have a better understanding of the ion transporting mechanism and can help optimize intercalation and storage of ions in battery materials.

SUPPLEMENTARY MATERIALS

Supplementary material for this article is available at http://advances.sciencemag.org/cgi/content/full/7/22/eabf0812/DC1

REFERENCES AND NOTES

1. M. Kühne, F. Börrnert, S. Fecher, M. Ghorbani-Asl, J. Biskupek, D. Samuelis, A. V. Krasheninnikov, U. Kaiser, J. H. Smet, Reversible superdense ordering of lithium between two graphene sheets. *Nature* **564**, 234–239 (2018).
2. T. Ohzuku, Y. Iwakoshi, K. Sawai, Formation of lithium-graphite intercalation compounds in nonaqueous electrolytes and their application as a negative electrode for a lithium ion (shuttlecock) cell. *J. Electrochem. Soc.* **140**, 2490–2498 (1993).
3. L. N. Wang, A. Menakath, F. Han, Y. Wang, P. Y. Zavalij, K. J. Gaskell, O. Borodin, D. Iuga, S. P. Brown, C. Wang, K. Xu, B. W. Eichhorn, Identifying the components of the solid-electrolyte interphase in Li-ion batteries. *Nat. Chem.* **11**, 789–796 (2019).
4. R. C. Asher, S. A. Wilson, Lamellar compound of sodium with graphite. *Nature* **181**, 409–410 (1958).
5. G. E. Pascal, M. Fouletier, Electrochemical intercalation of sodium in graphite. *Solid State Ion.* **28-30**, 1172–1175 (1988).
6. Y. J. Fang, D. Y. Luan, X. W. Lou, Recent advances on mixed metal sulfides for advanced sodium-ion batteries. *Adv. Mater.* **32**, e2002976 (2020).
7. M. S. Islam, C. A. J. Fisher, Lithium and sodium battery cathode materials: Computational insights into voltage, diffusion and nanostructural properties. *Chem. Soc. Rev.* **43**, 185–204 (2014).
8. G. Wang, F. Wang, P. Zhang, J. Zhang, T. Zhang, K. Müllen, X. Feng, Polarity-switchable symmetric graphite batteries with high energy and high power densities. *Adv. Mater.* **30**, 1802949 (2018).
9. B. Jache, P. Adelhelm, Use of graphite as a highly reversible electrode with superior cycle life for sodium-ion batteries by making use of co-intercalation phenomena. *Angew. Chem. Int. Ed.* **53**, 10169–10173 (2014).
10. J. Zhao, X. X. Zou, Y. J. Zhu, Y. H. Xu, C. S. Wang, Electrochemical intercalation of potassium into graphite. *Adv. Funct. Mater.* **26**, 8103–8110 (2016).
11. Y. Wen, K. He, Y. Zhu, F. Han, Y. Xu, I. Matsuda, Y. Ishii, J. Cumings, C. Wang, Expanded graphite as superior anode for sodium-ion batteries. *Nat. Commun.* **5**, 4033 (2014).
12. L. Seidl, L. Seidl, N. Bucher, E. Chu, S. Hartung, S. Martens, O. Schneider, U. Stimming, Intercalation of solvated Na-ions into graphite. *Energ. Environ. Sci.* **10**, 1631–1642 (2017).
13. H. Kim, J. Hong, Y. U. Park, J. Kim, I. Hwang, K. Kang, Sodium storage behavior in natural graphite using ether-based electrolyte systems. *Adv. Funct. Mater.* **25**, 534–541 (2015).
14. J. H. Sun, A. Iakunkov, A. T. Rebrikova, A. V. Talyzin, Exactly matched pore size for the intercalation of electrolyte ions determined using the tunable swelling of graphite oxide in supercapacitor electrodes. *Nanoscale* **10**, 21386–21395 (2018).
15. G. Yoon, H. Kim, I. Park, K. Kang, Conditions for reversible Na intercalation in graphite: Theoretical studies on the interplay among guest ions, solvent, and graphite host. *Adv. Energy Mater.* **7**, 1601519 (2017).

16. Y. Y. Liu, B. V. Merinov, W. A. Goddard, Origin of low sodium capacity in graphite and generally weak substrate binding of Na and Mg among alkali and alkaline earth metals. *Proc. Natl. Acad. Sci. U.S.A.* **113**, 3735–3739 (2016).
17. J. Xu, Recent progress in graphite intercalation compounds for rechargeable metal (Li, Na, K, Al)-ion batteries. *Adv. Sci.* **4**, 1700146 (2017).
18. W. Xu, M. M. Lerner, A new and facile route using electride solutions to intercalate alkaline earth ions into graphite. *Chem. Mater.* **30**, 6930–6935 (2018).
19. L. M. Zhang, J. W. Yu, M. M. Yang, Q. Xie, H. L. Peng, Z. F. Liu, Janus graphene from asymmetric two-dimensional chemistry. *Nat. Commun.* **4**, 1443 (2013).
20. Q. H. Wang, Z. Jin, K. K. Kim, A. J. Hilmer, G. L. C. Paulus, C.-J. Shih, M.-H. Ham, J. D. Sanchez-Yamagishi, K. Watanabe, T. Taniguchi, J. Kong, P. Jarillo-Herrero, M. S. Strano, Understanding and controlling the substrate effect on graphene electron-transfer chemistry via reactivity imprint lithography. *Nat. Chem.* **4**, 724–732 (2012).
21. Z. Xia, F. Leonardi, M. Gobbi, Y. Liu, V. Bellani, A. Liscio, A. Kovtun, R. Li, X. Feng, E. Orgiu, P. Samorì, E. Treossi, V. Palermo, Electrochemical functionalization of graphene at the nanoscale with self-assembling diazonium salts. *ACS Nano* **10**, 7125–7134 (2016).
22. J. H. Sun, M. A. Memon, W. Bai, L. Xiao, B. Zhang, Y. Jin, Y. Huang, J. Geng, Controllable fabrication of transparent macroporous graphene thin films and versatile applications as a conducting platform. *Adv. Funct. Mater.* **25**, 4334–4343 (2015).
23. Y. Wang, S. W. Tong, X. F. Xu, B. Ozyilmaz, K. P. Loh, Interface engineering of layer-by-layer stacked graphene anodes for high-performance organic solar cells. *Adv. Mater.* **23**, 1514–1518 (2011).
24. C. Casiraghi, Raman spectroscopy of graphene, in *Spectroscopic Properties of Inorganic and Organometallic Compounds* (2012), pp. 29–56.
25. K. Parvez, Z.-S. Wu, R. Li, X. Liu, R. Graf, X. Feng, K. Müllen, Exfoliation of graphite into graphene in aqueous solutions of inorganic salts. *J. Am. Chem. Soc.* **136**, 6083–6091 (2014).
26. Z. S. Wu, Y. Sun, Y. Z. Tan, S. B. Yang, X. L. Feng, K. Mullen, Three-dimensional graphene-based macro- and mesoporous frameworks for high-performance electrochemical capacitive energy storage. *J. Am. Chem. Soc.* **134**, 19532–19535 (2012).
27. H. W. Kim, H. W. Yoon, S. M. Yoon, M. B. Yoo, B. K. Ahn, Y. H. Cho, H. J. Shin, H. Yang, U. Paik, S. Kwon, J. Y. Choi, H. B. Park, Selective gas transport through few-layered graphene and graphene oxide membranes. *Science* **342**, 91–95 (2013).
28. J. H. Sun, A. Klechikov, C. Moise, M. Prodana, M. Enachescu, A. V. A. Talyzin, A molecular pillar approach to grow vertical covalent organic framework nanosheets on graphene: Hybrid materials for energy storage. *Angew. Chem. Int. Ed.* **57**, 1034–1038 (2018).
29. J. Sun, F. Morales-Lara, A. Klechikov, A. V. Talyzin, I. A. Baburin, G. Seifert, F. Cardano, M. Baldrighi, M. Frasconi, S. Giordani, Porous graphite oxide pillared with tetrapod-shaped molecules. *Carbon* **120**, 145–156 (2017).
30. M. S. Dresselhaus, G. Dresselhaus, Intercalation compounds of graphite. *Adv. Phys.* **51**, 1–186 (2002).
31. A. Ramos, I. Camean, N. Cuesta, C. Antuna, A. B. Garcia, Expanded graphitic materials prepared from micro- and nanometric precursors as anodes for sodium-ion batteries. *Electrochim. Acta* **187**, 496–507 (2016).
32. K. Ni, X. Wang, Z. Tao, J. Yang, N. Shu, J. Ye, F. Pan, J. Xie, Z. Tan, X. Sun, J. Liu, Z. Qi, Y. Chen, X. Wu, Y. Zhu, In operando probing of lithium-ion storage on single-layer graphene. *Adv. Mater.* **31**, 1808091 (2019).
33. W. Tang, B. M. Goh, M. Y. Hu, C. Wan, B. Tian, X. Deng, C. Peng, M. Lin, J. Z. Hu, K. P. Loh, In situ raman and nuclear magnetic resonance study of trapped lithium in the solid electrolyte interface of reduced graphene oxide. *J. Phys. Chem. C* **120**, 2600–2608 (2016).
34. E. Pollak, B. Geng, K. J. Jeon, I. T. Lucas, T. J. Richardson, F. Wang, R. Kostecki, The interaction of Li+ with single-layer and few-layer graphene. *Nano Lett.* **10**, 3386–3388 (2010).
35. J. H. Sun, L. H. Xiao, S. D. Jiang, G. X. Li, Y. Huang, J. X. Geng, Fluorine-doped SnO2@ graphene porous composite for high capacity lithium-ion batteries. *Chem. Mater.* **27**, 4594–4603 (2015).
36. C. Wang, H. Wu, Z. Chen, M. T. McDowell, Y. Cui, Z. A. Bao, Self-healing chemistry enables the stable operation of silicon microparticle anodes for high-energy lithium-ion batteries. *Nat. Chem.* **5**, 1042–1048 (2013).
37. Z. Li, J. T. Zhang, Y. Lu, X. W. Lou, A pyrolyzed polyacrylonitrile/selenium disulfide composite cathode with remarkable lithium and sodium storage performances. *Sci Adv* **4**, eaat1687 (2018).
38. A. Ponrouch, R. Dedryvère, D. Monti, A. E. Demet, J. M. Ateba Mba, L. Croguennec, C. Masquelier, P. Johansson, M. R. Palacín, Towards high energy density sodium ion batteries through electrolyte optimization. *Energ. Environ. Sci.* **6**, 2361–2369 (2013).
39. N. Weadock, N. Varongchayakul, J. Y. Wan, S. Lee, J. Seog, Determination of mechanical properties of the SEI in sodium ion batteries via colloidal probe microscopy. *Nano Energy* **2**, 713–719 (2013).
40. P. Verma, P. Maire, A review of the features and analyses of the solid electrolyte interphase in Li-ion batteries. *Electrochim. Acta* **55**, 6332–6341 (2010).
41. M. Inaba, H. Yoshida, Z. Ogumi, T. Abe, Y. Mizutani, M. Asano, In situ Raman study on electrochemical li intercalation into graphite. *J. Electrochem. Soc.* **142**, 20–26 (1995).
42. M. A. Reddy, M. Helen, A. Gross, M. Fichtner, H. Euchner, Insight into sodium insertion and the storage mechanism in hard carbon. *Acs Energy Lett.* **3**, 2851–2857 (2018).
43. X. Z. Shu, M. Zhang, Y. He, H. Frei, F. D. Toste, Dual visible light photoredox and gold-catalyzed arylative ring expansion. *J. Am. Chem. Soc.* **136**, 5844–5847 (2014).
44. D. Pierleoni, M. Minelli, S. Ligi, M. Christian, S. Funke, N. Reineking, V. Morandi, F. Doghieri, V. Palermo, Selective gas permeation in graphene oxide–polymer self-assembled multilayers. *ACS Appl. Mater. Interfaces* **10**, 11242–11250 (2018).
45. A. Iakunkov, A. Klechikov, J. Sun, T. Steenhaut, S. Hermans, Y. Filinchuk, A. Talyzin, Gravimetric tank method to evaluate material-enhanced hydrogen storage by physisorbing materials. *Phys. Chem. Chem. Phys.* **20**, 27983–27991 (2018).
46. G. Kresse, Ab-initio molecular-dynamics for liquid-metals. *J. Non Cryst. Solids* **192-193**, 222–229 (1995).
47. G. Kresse, J. Furthmuller, Efficient iterative schemes forab initio total-energy calculations using a plane-wave basis set. *Phys. Rev. B* **54**, 11169–11186 (1996).
48. G. Kresse, J. Furthmüller, Efficiency of ab-initio total energy calculations for metals and semiconductors using a plane-wave basis set. *Comp. Mater. Sci.* **6**, 15–50 (1996).
49. G. Kresse, D. Joubert, From ultrasoft pseudopotentials to the projector augmented-wave method. *Phys. Rev. B* **59**, 1758–1775 (1999).
50. P. E. Blochl, Projector augmented-wave method. *Phys. Rev. B* **50**, 17953–17979 (1994).
51. J. P. Perdew, K. Burke, M. Ernzerhof, Generalized gradient approximation made simple. *Phys. Rev. Lett.* **77**, 3865–3868 (1996).
52. S. Grimme, J. Antony, S. Ehrlich, H. Krieg, A consistent and accurate ab initio parametrization of density functional dispersion correction (DFT-D) for the 94 elements H-Pu. *J. Chem. Phys.* **132**, 154104 (2010).
53. S. R. Bahn, K. W. Jacobsen, An object-oriented scripting interface to a legacy electronic structure code. *Comput. Sci. Eng.* **4**, 56–66 (2002).
54. R. F. W. Bader, *Atoms in Molecules: A Quantum Theory* (Oxford Univ. Press, 1994).
55. W. Tang, E. Sanville, G. Henkelman, A grid-based Bader analysis algorithm without lattice bias. *Condens. Matter* **21**, 084204 (2009).
56. E. Bekyarova, M. E. Itkis, P. Ramesh, C. Berger, M. Sprinkle, W. A. de Heer, R. C. Haddon, Chemical modification of epitaxial graphene: Spontaneous grafting of aryl groups. *J. Am. Chem. Soc.* **131**, 1336–1337 (2009).
57. Z. Tehrani, G. Burwell, M. A. M. Azmi, A. Castaing, R. Rickman, J. Almarashi, P. Dunstan, A. M. Beigi, S. H. Doak, O. J. Guy, Generic epitaxial graphene biosensors for ultrasensitive detection of cancer risk biomarker. *2d Mater* **1**, 025004 (2014).
58. M. M. Lucchese, F. Stavale, E. H. M. Ferreira, C. Vilani, M. V. O. Moutinho, R. B. Capaz, C. A. Achete, A. Jorio, Quantifying ion-induced defects and Raman relaxation length in graphene. *Carbon* **48**, 1592–1597 (2010).

Acknowledgments: We thank V. Bellani for the useful discussion on the Raman data analysis, as well as P. Vana, F. Ehlers and J. Berlin for providing technical equipment. **Funding:** The research leading to these results has received funding from the European Union's Horizon 2020 research and innovation program under GrapheneCore3 881603–Graphene Flagship, FLAG-ERA project PROSPECT, and from the Swedish Research Council under project Janus 2017-04456. The calculations were performed at C3SE (Göteborg) through an SNIC grant. This work was performed, in part, at Myfab Chalmers and Chalmers materials analysis laboratory.
Author contributions: J.S. and V.P. conceived and designed the experiments. J.S. prepared and characterized the samples. J.S. and R.Q. did the TEM characterization. H.G. and P.E. performed the DFT calculation. M.S., J.S., and A.M. discussed and did the operando Raman spectroelectrochemical characterization. Z.X. contributed to the Raman analysis, V.Q. contributed to the ion transport setup. J.S. and P.H.T. performed ellipsometry imaging characterization. J.S. and V.P. prepared the manuscript. All authors discussed the results and commented on the manuscript. **Competing interests:** The authors declare that they have no competing interests. **Data and materials availability:** All data needed to evaluate the conclusions in the paper are present in the paper and/or the Supplementary Materials. Additional data related to this paper may be requested from the authors.

Submitted 2 October 2020
Accepted 9 April 2021
Published 28 May 2021
10.1126/sciadv.abf0812

Citation: J. Sun, M. Sadd, P. Edenborg, H. Grönbeck, P. H. Thiesen, Z. Xia, V. Quintano, R. Qiu, A. Matic, V. Palermo, Real-time imaging of Na^+ reversible intercalation in "Janus" graphene stacks for battery applications. *Sci. Adv.* **7**, eabf0812 (2021).

Real-time imaging of Na^+ reversible intercalation in "Janus" graphene stacks for battery applications

Jinhua Sun, Matthew Sadd, Philip Edenborg, Henrik Grönbeck, Peter H. Thiesen, Zhenyuan Xia, Vanesa Quintano, Ren Qiu, Aleksandar Matic and Vincenzo Palermo

Sci Adv **7** (22), eabf0812.
DOI: 10.1126/sciadv.abf0812